

Yiting Xie ; Matthew D. Cham ; Claudia Henschke ; David Yankelevitz ; Anthony P. Reeves; Automated coronary artery calcification detection on low-dose chest CT images. Proc. SPIE 9035, Medical Imaging 2014: Computer-Aided Diagnosis, 90350F (March 20, 2014);

doi:10.1117/12.2043840.

© (2014) COPYRIGHT Society of Photo-Optical Instrumentation Engineers (SPIE). Downloading of the paper is permitted for personal use only. Systematic or multiple reproduction, duplication of any material in this paper for a fee or for commercial purposes, or modification of the content of the paper are prohibited.

# Automated coronary artery calcification detection on low-dose chest CT images

Yiting Xie<sup>a</sup>, Matthew D. Cham<sup>b</sup>, Claudia Henschke<sup>b</sup>, David Yankelevitz<sup>b</sup> and Anthony P. Reeves<sup>a</sup>

<sup>a</sup>School of Electrical and Computer Engineering, Cornell University, Ithaca, NY, USA

<sup>b</sup>Department of Radiology, Icahn School of Medicine at Mount Sinai, New York, NY, USA

## ABSTRACT

Coronary artery calcification (CAC) measurement from low-dose CT images can be used to assess the risk of coronary artery disease. A fully automatic algorithm to detect and measure CAC from low-dose non-contrast, non-ECG-gated chest CT scans is presented. Based on the automatically detected CAC, the Agatston score (AS), mass score and volume score were computed. These were compared with scores obtained manually from standard-dose ECG-gated scans and low-dose un-gated scans of the same patient.

The automatic algorithm segments the heart region based on other pre-segmented organs to provide a coronary region mask. The mitral valve and aortic valve calcification is identified and excluded. All remaining voxels greater than 180HU within the mask region are considered as CAC candidates.

The heart segmentation algorithm was evaluated on 400 non-contrast cases with both low-dose and regular dose CT scans. By visual inspection, 371 (92.8%) of the segmentations were acceptable. The automated CAC detection algorithm was evaluated on 41 low-dose non-contrast CT scans. Manual markings were performed on both low-dose and standard-dose scans for these cases. Using linear regression, the correlation of the automatic AS with the standard-dose manual scores was 0.86; with the low-dose manual scores the correlation was 0.91. Standard risk categories were also computed. The automated method risk category agreed with manual markings of gated scans for 24 cases while 15 cases were 1 category off. For low-dose scans, the automatic method agreed with 33 cases while 7 cases were 1 category off.

**Keywords:** heart segmentation, coronary artery calcification measurement, automated computer algorithm, low-dose non-contrast CT

## 1. INTRODUCTION

This paper presents a fully automated algorithm to segment the heart region and detect coronary artery calcification (CAC) from low-dose, non-contrast, non-ECG-gated chest CT scans. It has been shown that CT is an accurate method to quantify coronary plaque burden and calcification measurements on CT correlate well with histological analyses [1]. Shemesh et al. [2] have shown that CAC score can be derived from un-gated low-dose MDCT images and this information can contribute to risk stratification of coronary artery disease. Shemesh et al. [3] have also shown that visual assessment of CAC on low-dose CT scans provides clinically relevant information for predicting the risk of cardiovascular death.

An anatomy-based approach is employed for heart segmentation. It is similar to the algorithm presented by Reeves et al. [4] but with an improved pre-segmentation of adjacent organs. In previous work, Isgum et al. [5] performed heart segmentation in low-dose non-contrast CT images using a multi-atlas based approach. They also performed CAC detection and measurement in low-dose CT images in [6], [7] and [8] using the geometrical and spatial features of CAC. Compared to that work, the method in this paper does not require manually segmented templates, thus making the algorithm more efficient and easier to extend to larger datasets.

## 2. METHODS

Heart segmentation from low-dose non-contrast CT scans is very challenging due to the presence of image noise and the lack of intensity changes between heart region and adjacent tissues. To achieve robust segmentation our algorithm models the heart as an entity spatially enclosed by other well-defined anatomical entities. By robustly identifying the surrounding entities, the remaining enclosed region is considered as the heart region. This method builds on the approach presented in [4], in which heart region was segmented based on the pre-segmented bone, airways, lungs as well as the estimated diaphragm. The new method, in addition, employs the pre-segmented aorta, fatty tissue and pulmonary artery, thus better capturing the location of heart. Some of the entities can be directly obtained from the pre-computed Anatomy Label Map (ALM), a robust chest segmentation infrastructure developed by the Cornell VIA group [9]. The pre-segmented organs include airways [10], lungs [11], bone [12], aorta [13] and fatty tissue [14]. Heart segmentation involves the following steps:

- (1) Obtain the pre-segmented lung, bone and fatty tissue. Together they provide constraints to the heart region from left, right, anterior and posterior sides (see Figure 1).
- (2) Compute the location of the top of diaphragm similarly as in [4] by analyzing lung profiles. The top of the diaphragm is considered as the inferior margin of the heart.
- (3) Obtain the pre-segmented aorta. The descending aorta provides further constraint to the posterior margin of the heart.
- (4) Based on the segmented aorta, the general location of the pulmonary artery is estimated. Using the estimated pulmonary artery, the superior margin of the heart is determined.
- (5) Using all the constraints in step (1) - (4), limit heart location to the enclosed unlabeled region. Then select the largest connected component as the segmented heart.

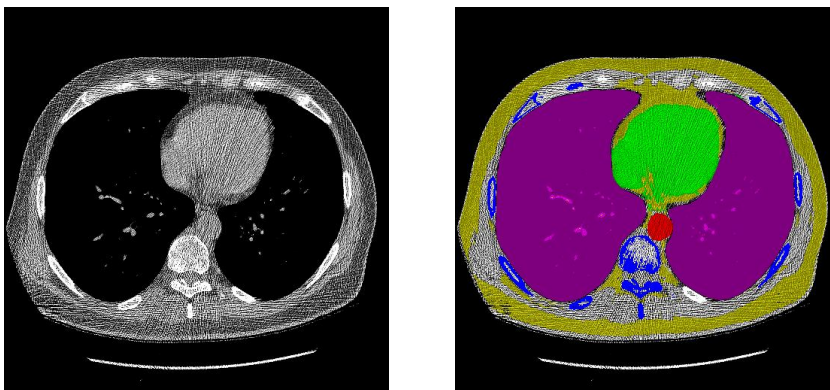


Figure 1. Left: original CT scan; right: segmented anatomical entities overlaid on the original image, lungs in magenta, bone in blue, aorta in red, fatty tissue in yellow and heart region in green.

Step (1) provides robust constraint to heart location while step (2), (3) and (4) are approximations of superior and inferior margins of the heart due to lack of boundary evidence in low-dose images. Step (5) is used to eliminate the voxels outside the actual heart region. In step (4), the pulmonary artery location is estimated by the following algorithm:

- (1) Determine the left right extent of pulmonary artery based on the left right extent of the aorta.
- (2) Consider the CT image from the sagittal viewpoint. In the leftmost sagittal plane of pulmonary artery, identify a seed point inside the pulmonary artery lumen by fitting the largest circle into the unlabeled region shown in figure 2(a) and 2(c). The center of the largest circle is the desired seed point. Similarly, in the rightmost sagittal plane, find a seed point inside its lumen by largest circle fitting into the unlabeled region in figure 2(b) and 2(e).
- (3) By connecting the two seed points to form a centerline, the general location of the pulmonary artery is constrained. Then based on the two largest circles, the radius of pulmonary artery is estimated. The centerline and radius will determine a cylinder, which is used to represent the pulmonary artery (see figure 2(d)).

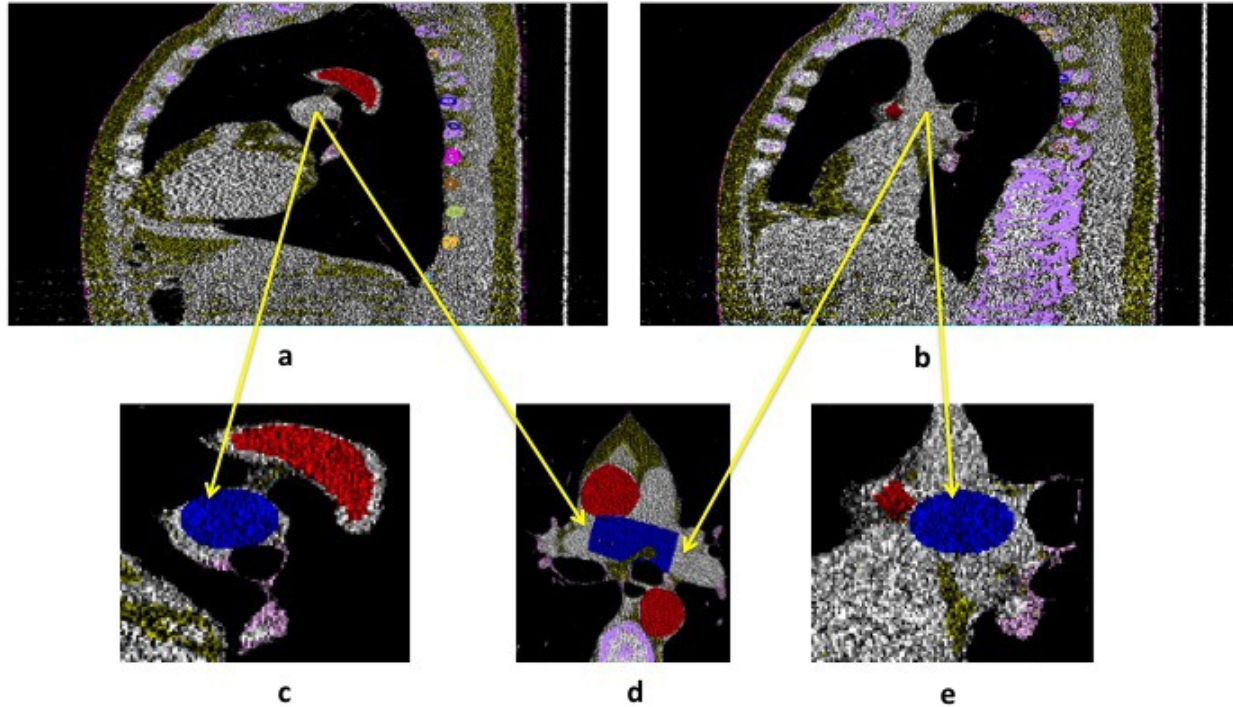


Figure 2. Illustration of pulmonary artery estimation. In all five images the segmented organs are overlaid on the original CT image in different colors. a and b are respectively the two sagittal slices containing the left and right seed points. c and e correspond to a and b respectively. They contain the largest circle (blue) fit into the region of interest as well as aorta (red) fatty tissues (yellow) airway (light purple below aorta) and bony structures (multiple colors). d shows the estimated pulmonary artery (blue) with aorta, airway and bones. Note that all images are in anisotropic space.

This method is only able to estimate the general location and shape of the pulmonary artery. However it is sufficient to constrain the superior margin of the heart region. Figure 3 shows examples of segmented heart with segmented aorta, lungs, bone and estimated pulmonary artery in coronary and sagittal views.

Based on the segmented heart, the detection of CAC is performed using the following algorithm:

- (1) Slightly enlarge heart region by dilation to include pericardial region to obtain a coronary region that encloses all coronary arteries.
- (2) Filter the original CT image using a filter  $F=3 \times 3 \times 3$  mean and threshold it at intensity value  $I=180HU$ . Apply the coronary mask to the processed image to obtain potential coronary calcification candidates. Select calcified voxels with a size larger than  $n=5$  voxels.
- (3) Determine the approximate aortic valve region by projecting the segmented aorta through heart and eliminate all calcification in that region as aortic valve calcification.
- (4) Determine the approximate mitral valve region by searching the left posterior quadrant of heart. Eliminate all calcification candidates larger than  $m=1000$  voxels in this region as mitral valve calcification.

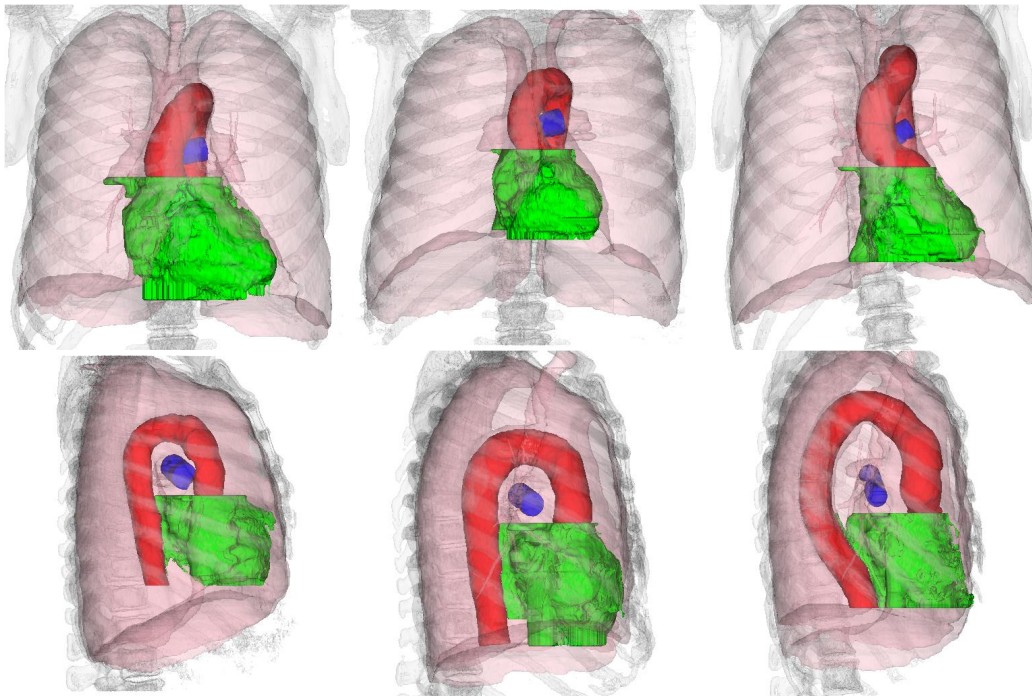


Figure 3. 3D visualization of segmented heart region (green), aorta (red), pulmonary artery (blue), lungs (light pink) and bone (light grey) from 3 different cases. Top row shows the coronary view while bottom row shows the sagittal view of the corresponding case.

Step (1), (3) and (4) are designed to find the potential spatial regions for possible CAC while eliminating calcification that does not belong to CAC. Step (2) is designed to deal with the high level of noise present in low-dose CT images. Figure 4 compares the CAC detection results using different filters  $F$  and threshold  $I$ . It is observed that with standard calcium threshold 130HU and no pre-filtering of the images, most detected CAC are actually noise pixels (No filtering,  $I=130HU$ ). A mean filter of size  $3 \times 3 \times 3$  is able to eliminate most noise voxels with only losing a few true CAC voxels in the superior heart region, but in the inferior heart region where the noise level is even higher, a lot of noise voxels are still mis-identified as CAC ( $F=3 \times 3 \times 3$  mean,  $I=130HU$ ). Eventually, with pre-filtering and an elevated threshold of 180HU, almost all noise voxels are eliminated while the majority of CAC voxels are still preserved ( $F=3 \times 3 \times 3$  mean,  $I=180HU$ ).

Since neither the mitral valve nor the aortic valve region can be visually distinguished from surrounding tissues in non-contrast scans, their locations can only be approximated. The pre-segmented aorta typically does not extend to the aortic valve region. However, the aortic valve is usually located a short distance below the end of the ascending aorta. It was also observed that this region does not contain coronary arteries. Therefore, the segmented ascending aorta is projected down through the heart region and all calcifications covered by the projection are eliminated. Similarly, calcifications in the mitral valve region can be eliminated by searching the left posterior quadrant of heart. Since mitral valve calcification usually has a much larger volume than CAC, only calcification larger than 1,000 voxels is eliminated. Figure 5 shows the detection of true CAC and the elimination of aortic valve and mitral valve calcification. Figure 5(a), 5(b) belong to one case and 5(e), 5(f) are their corresponding 3D visualizations. 5(a) shows the superior heart region with true CAC (yellow arrow) while 5(b) shows the aortic valve (red arrow) and mitral valve (orange arrow) calcification. 5(e) shows all the calcification detected in the enlarged heart region while 5(f) shows the final detected CAC after elimination of false calcification. Figure 5(c), 5(d) shows the true CAC in different heart regions.

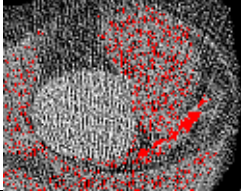
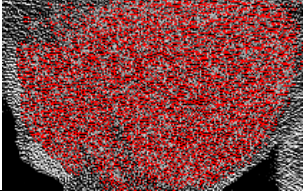
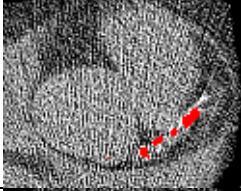
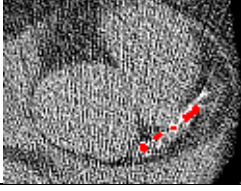
$F, I$	Superior Heart Region (With CAC)	Inferior Heart Region (Without CAC)
Original Image		
No filtering, $I=130\text{HU}$		
$F=3\times 3\times 3$ mean, $I=130\text{HU}$		
$F=3\times 3\times 3$ mean, $I=180\text{HU}$		

Figure 4. Effect of different filter  $F$  and threshold  $I$  on detected CAC results. CAC voxels are in red and overlaid on the original images.

### 3. EXPERIMENT AND RESULTS

The heart segmentation algorithm was evaluated on 3 datasets. The first dataset contains 41 low-dose non-contrast chest CT scans. The second is the public VIA-ELCAP [15, 16] dataset, which contains 45 low-dose non-contrast chest CT scans. The third is a subset of the public LIDC [17] dataset, which contains 335 non-contrast chest CT scans with both low-dose and standard-dose scans. Only 314 non-contrast scans from LIDC dataset were used, however, and the remaining 21 scans were discarded due to extreme image artifacts or abnormal anatomical structures. Visual inspection was used for evaluation. For each segmentation result, a 2D and 3D visualization of the heart region together with other organs was computed similarly to figure 1 and figure 3. Inspection showed that: for the first and second dataset, all heart segmentation had good result, i.e. the heart region was correctly captured without visible non-heart tissues attached to it. For the third dataset, 285 of the 314 cases were good while in the other 29 cases, the segmented heart was not well constrained. More details in heart segmentation have been given in the discussion section.

The CAC detection and measurement algorithm was tested on 41 low-dose non-contrast chest CT scans. All 41 scans were performed at 120kVp, 40mAs. Each scan has its respective standard-dose ECG-gated scan of the same patient taken within a short time interval. Both the low-dose and the standard-dose scans have manual markings of CAC. The automatically detected CAC was compared with both markings. Manual scores on the standard-dose scans were obtained by extracting all voxels with an intensity value greater than 130HU in the marked regions. Manual scores on the low-dose scans were obtained by mean filtering the intensity image using a 3x3x3 filter and extracting all voxels with an intensity value greater than 130HU in the marked regions. The standard threshold of 130HU was used since the manual markings only enclosed the calcification regions. Therefore the standard (lower) threshold would preserve as many true CAC voxels as possible without capturing many false positive CAC voxels.

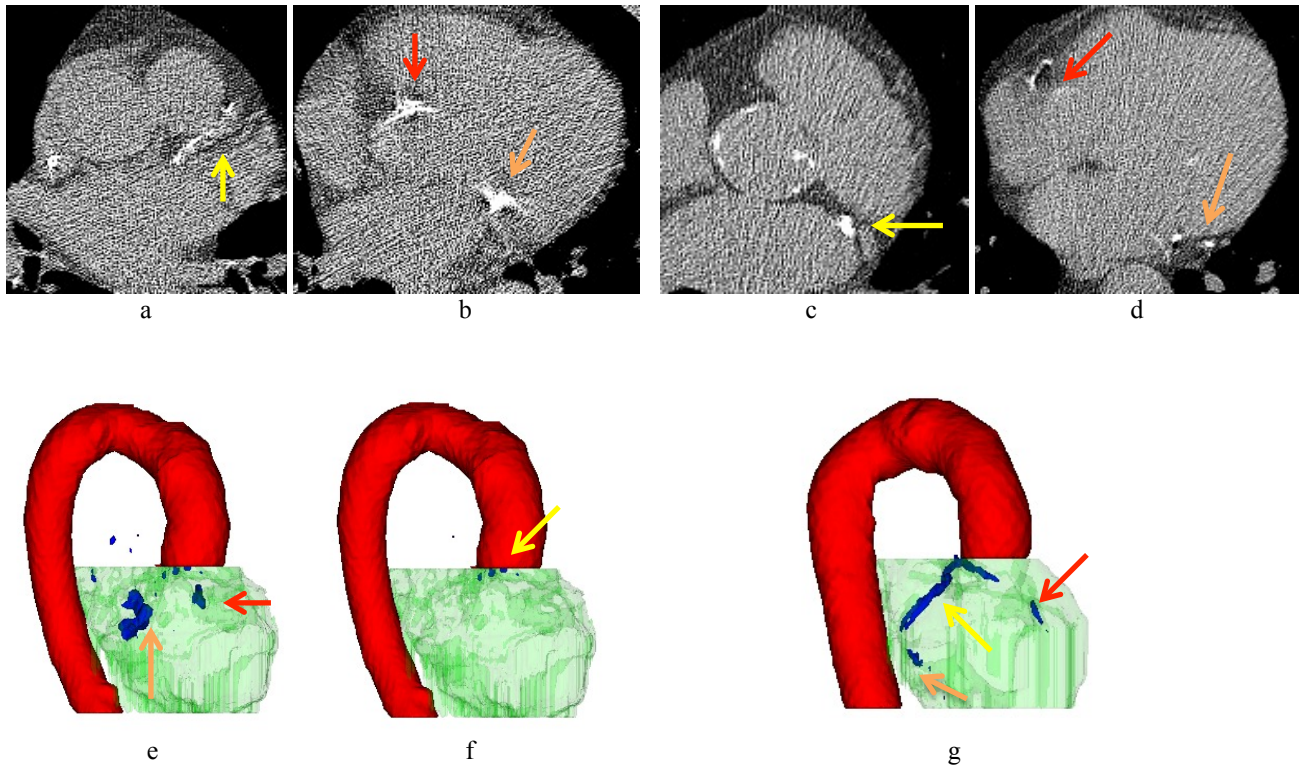


Figure 5. Illustration of original scan images and detected CAC (blue), segmented heart (light green) and segmented aorta (red) in a sagittal view. (a) and (b) belong to one case. (e) is the 3D visualization of detected calcification in the heart region and (f) is the same case after elimination of aortic valve and mitral valve calcification. (c) and (d) belong to a second case. (g) is the corresponding 3D visualization.

Two evaluation metrics comparing between automated and manual CAC measurements were considered: the first metric was the linear regression correlation coefficient R-squared between the automated Agatston score and the manual Agatston score; the second metric was to compare the resulting risk categories of the different methods for each case. Risk category corresponds to the Agatston score (AS) in the following way: risk level 1 (low risk):  $AS \in [0,10]$ ; risk level 2 (moderate risk):  $AS \in [11,100]$ ; risk level 3 (moderately high risk):  $AS \in [101,400]$ ; risk level 4 (high risk):  $AS > 400$ .

Based on CAC measurement results, the automated AS has a mean of 232, a minimum of 0 and a maximum of 2405. Log transform was performed on all scores before computing the correlation coefficients. The automated AS had a correlation of 86% with the manual AS from the standard-dose scans and a correlation of 91% with the manual AS from the low-dose scans as shown in figure 6. The automated volume and mass scores were respectively 86% and 84% correlated with the standard-dose volume and mass scores and 90% and 80% correlated with the low-dose manual volume and mass scores. Compared to risk categories assigned by the standard-dose manual markings, the automated algorithm correctly assigned the risks of 24 cases (59%) while 15 cases (37%) were one category off. Compared to risk categories assigned by the low-dose manual markings, the automated algorithm correctly assigned the risks of 33 cases (80%) while 7 cases (17%) were one category off. Figure 7 shows the CAC distributions using automated method, manual method on standard-dose and low-dose images. Table 1 shows the confusion matrices between manual and automated methods.

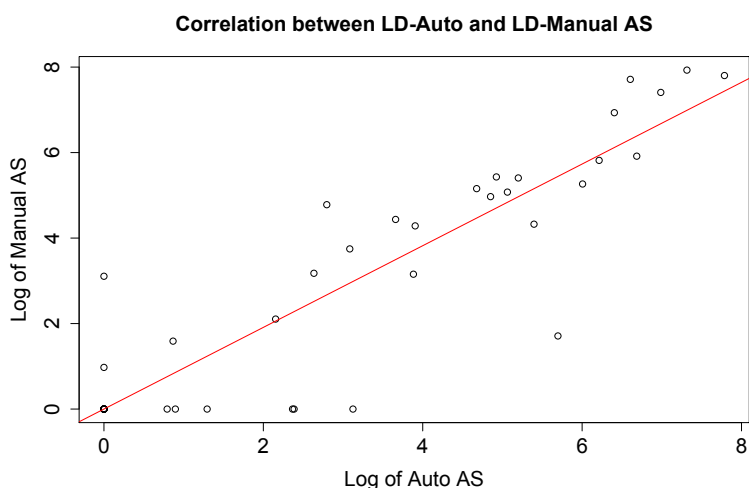
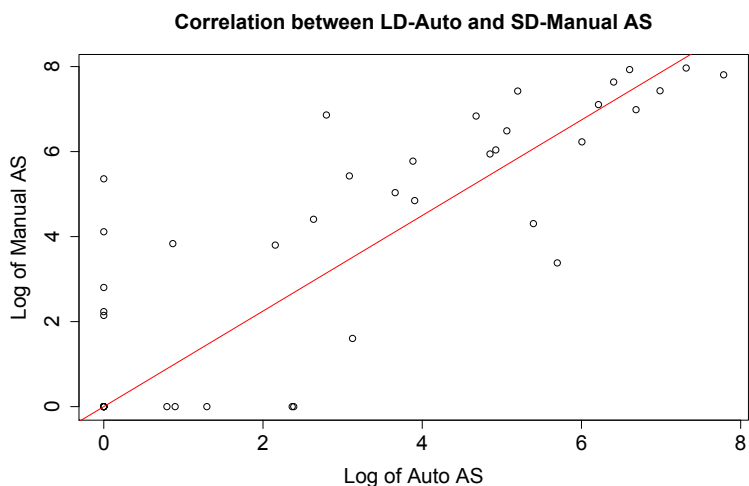


Figure 6. Linear regression correlation between automated AS and manual AS. Upper graph shows the correlation between automated AS on low-dose images (LD-Auto) and manual AS on standard-dose images (SD-Manual). Lower graph shows the correlation between automated AS on low-dose images (LD-Auto) and manual AS on low-dose images (LD-Manual). Red line is the regression line fit to the data points.

Table 1. CM1: confusion matrix between low-dose automatic method (LD-Auto) and standard-dose manual method (SD-Manual). CM2: confusion matrix between LD-Auto and low-dose manual method (LD-Manual). A1-A4 stands for risk category 1-4 based on AS using automatic method. M1-M4 stands for risk category 1-4 based on AS using manual method.

CM1 (LD-Auto v.s. SD-Manual)	M1	M2	M3	M4	CM2 (LD-Auto v.s. LD-Manual)	M1	M2	M3	M4
A1	14	4	1	0	A1	18	1	0	0
A2	1	1	4	1	A2	1	5	1	0
A3	0	2	1	4	A3	1	1	5	0
A4	0	0	0	8	A4	0	0	3	5

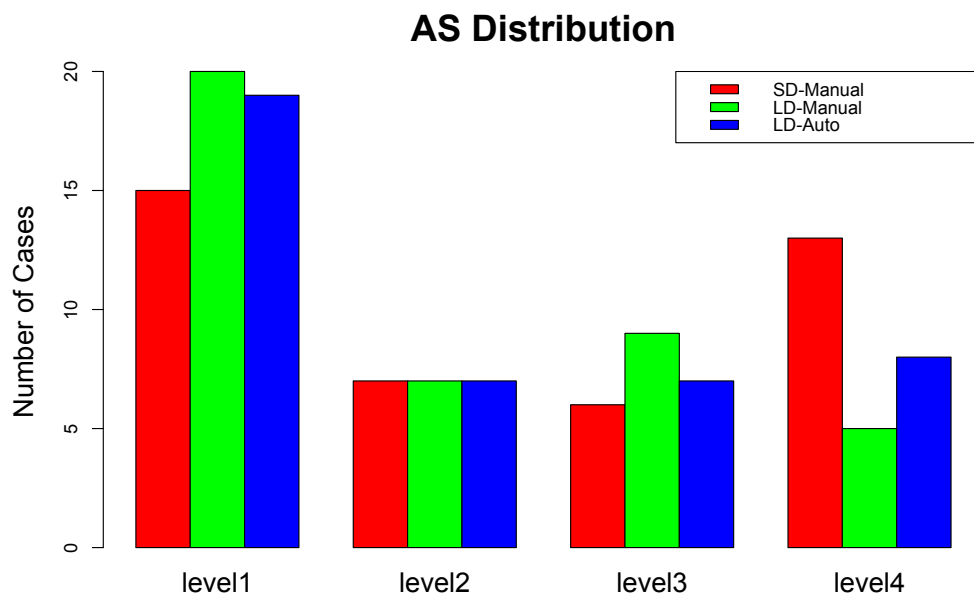


Figure 7. Agatston score (AS) using standard-dose manual markings (SD-Manual red), low-dose manual markings (LD-Manual green) and low-dose automatic method (LD-Auto blue). The 4 levels correspond to the 4 risk categories.

#### 4. DISCUSSION

The heart segmentation algorithm was able to produce good results such as in Figure 3 for 371 (92.8%) out of the 400 test cases. However, inaccurate segmentation occurred when adjacent organs were unable to provide a strong constraint for the heart as shown in figure 8. Among the 29 inaccurate heart segmentations, in 19 cases the heart region had inaccurate anterior and posterior boundaries (see figure 8(a) and (b)). In 10 cases the heart region had inaccurate inferior boundary caused by the inaccurate estimation of diaphragm or pulmonary artery location (see figure 8(c) and 8(d)). All 41 cases used for CAC evaluation, however, had accurate heart region segmentation. In future work, these issues will be addressed by more accurately segmenting adjacent organs.

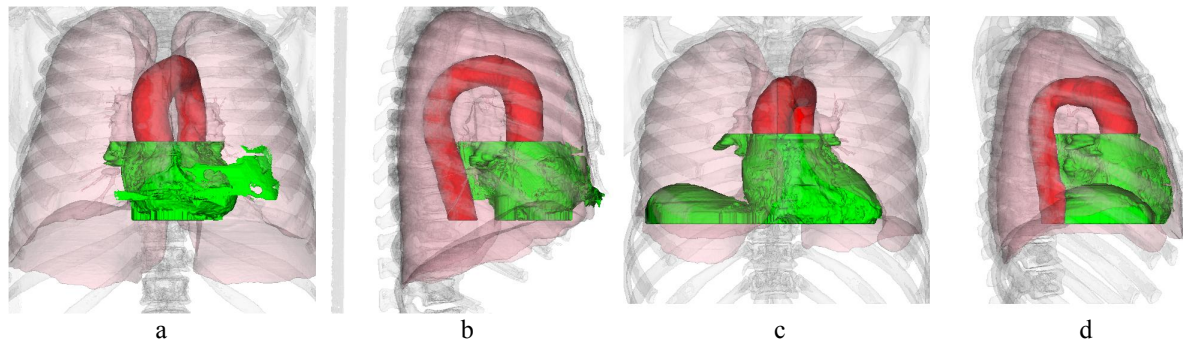


Figure 8. Examples of inaccurate heart segmentation from two cases. a and b belong to one case with non-heart tissues attached to heart. c and d belong to another case with incorrectly estimated diaphragm location.

The automatic CAC detection and measurement algorithm performed well compared to low-dose manual markings. Compared to standard-dose manual markings, however, it had a slightly lower accuracy. The main reason was that in low-dose images, it is very hard to distinguish small regions of CAC from noise voxels. This is also shown when comparing the low-dose manual markings with standard-dose manual markings. Using standard-dose markings as references, the low-dose markings were able to correctly assign the risk category of 23 cases (56%) while 8 cases (20%) were one category off.

## 5. CONCLUSION

This paper presents an automatic algorithm to segment the heart region and detect coronary artery calcification (CAC) for low-dose non-contrast CT scans. The heart segmentation algorithm performs well in 92.8% of the test cases. The detected and measured CAC has a high correlation with manually segmented CAC from both low-dose and corresponding standard dose scans. The automatic method is also able to correctly assign risk category for 80% of the cases compared to low-dose manual markings.

## ACKNOWLEDGEMENT

This study was supported by a grant from the Flight Attendant Medical Research Institute (FAMRI).

## REFERENCES

- [1] Thompson, B. H., and Stanford, W., "Update on using coronary calcium screening by computed tomography to measure risk for coronary heart disease." *Int. J. Cardiovasc. Imaging* 21(1), 39-53 (2005).
- [2] Shemesh, J., Henschke, C. I., Farooqi, A., Yip, R., Yankelevitz, D. F., Shaham, D. and Miettinen, O. S., "Frequency of coronary artery calcification on low-dose computed tomograph screening for lung cancer," *Clinical Imaging* 30(3), 181-185 (2006).
- [3] Shemesh, J., Henschke, C. I., Shaham, D., Yip, R., Farooqi A. O., Cham, M. D., McCauley, D. I., Chen, M., Smith, J. P., Libby, D. M., Pasmantier, M. W. and Yankelevitz, D. F., "Ordinal scoring of coronary artery calcification on low-dose CT scans of the chest is predictive of death from cardiovascular disease." *Radiology* 257(2), 541-548 (2010).
- [4] Reeves, A. P., Biancradi, A. M., Yankelevitz, D. F., Cham, M. D., and Henschke, C. I., "Heart region segmentation from low-dose CT scans: an anatomy based approach." *SPIE Med. Imaging* 8314, 83142A (2012).
- [5] Isgum, I., Staring, M., Rutten, A., Prokop, M., Viergever, M. A., and Van Ginneken, B., "Multi-atlas-based segmentation with local decision fusion-application to cardiac and aortic segmentation in CT scans." *IEEE Trans. Med. Imaging* 28(7), 1000-1010 (2009).
- [6] Isgum, I., Van Ginneken, B., and Prokop, M., "A pattern recognition approach to automated coronary calcium scoring." *Pattern Recognition* 3, 746-749 (2004).
- [7] Isgum, I., Van Ginneken, B., Rutten, A. and Prokop, M., "Automated coronary calcification detection and scoring." *ISPA* 127-132 (2005).
- [8] Isgum, I., Prokop, M., Niemeijer, M., Viergever, M. A., and Van Ginneken, B., "Automatic coronary calcium scoring in low-dose chest computed tomography." *IEEE Trans. Med Imaging* 31(12), 2322-2334 (2012).
- [9] *Vision and Image Analysis Group, Cornell University*, 13 May 2013 <[www.via.cornell.edu](http://www.via.cornell.edu)>.
- [10] Lee, J., Reeves, A. P., Fotin, S. V., Apanasovich, T., and Yankelevitz, D. F., "Human airway measurement from CT images." *SPIE Medical Imaging*. 6915, 691518 (2008).
- [11] Reeves, A. P., Chan, A. B., Yankelevitz, D. F., Henschke, C. I., Kressler, B., and Kostis, W. J., "On measuring the change in size of pulmonary nodules." *IEEE. Trans. Med. Imaging* 25(4), 435-450 (2006).
- [12] Lee, J., and Reeves, A. P., "Segmentation of individual ribs from low-dose chest CT." *SPIE Medical Imaging* 7624, 76243J (2010).
- [13] Xie, Y., Padgett, J., Biancardi, A. M., and Reeves, A. P., "Automated aorta segmentation in low-dose chest CT images." *IJCARS*, (2013).
- [14] Padegett, J., Biancardi, A. M., Henschke, C. I., Yankelevitz, D. F., and Reeves, A. P., "Local noise estimation in low-dose chest CT images." *IJCARS*, (2013).
- [15] *ELCAP Public Lung Image Database*, 13 May 2013 <[www.via.cornell.edu/databases/lungdb.html](http://www.via.cornell.edu/databases/lungdb.html)>.
- [16] Reeves, A. P., Biancardi, A. M., Yankelevitz, D. F., Fotin, S., Keller, B. M., Jiraptnakul, A. and Lee, J., "A Public Image Database to Support Research in Computer Aided Diagnosis." 31<sup>st</sup> Conf. IEEE EMBS, 3715-3718 (2009).
- [17] Armato, S. G., et al, "The Lung Image Database Consortium (LIDC) and Image Database Resource Initiative (IDRI): A Completed Reference Database of Lung Nodules on CT Scans," *Medical Physics* 38 (2), 915-931 (2011).